Angewandte Chemie International Edition
www.angewandte.org

How to cite: Angew. Chem. Int. Ed. 2025, e202500474
doi.org/10.1002/anie.202500474

VIP Single-Atom Catalyst | Very Important Paper

Three-Electron Uric Acid Oxidation via Interdistance-Dependent Switching Pathways in Correlated Single-Atom Catalysts for Boosting Sensing Signals

Bowen Jiang, Heng Zhang, Rui Pan, Min Ji, Lin Zhu, Guoju Zhang, Jing Liu, Huihui Shi, Huang Huang, Shu Wan, Kuibo Yin, and Litao Sun**

Abstract: The overly simplistic geometric and electronic structures of single-atom catalysts have become a significant bottleneck in the field of single-atom sensing, impeding both the design of highly efficient electrochemical sensors and the establishment of structure–activity relationships. To address these challenges, we present a novel strategy to boost the sensing performance of single-atom catalysts by precisely tuning the single-atomic interdistance (SAD) in correlated single-atom catalysts (*c*-SACs). A series of Ru-based *c*-SACs ($Ru_{d=6.2\,Å}$, $Ru_{d=7.0\,Å}$, and $Ru_{d=9.3\,Å}$) are synthesized with predetermined SAD values, which are comprehensively characterized by various techniques. Electrochemical studies on uric acid (UA) oxidation reveal that $Ru_{d=6.2\,Å}$ demonstrates an extraordinary sensitivity of 9.83 $\mu A\ \mu M^{-1}cm^{-2}$, which is superior to most of electrochemistry biosensors reported previously. Kinetic analysis and product examination unveil that the 6.2 Å Ru SAD instigates a distinctive three-electron oxidation of UA, with an extra electron transfer compared to the conventional two-electron pathway, which fundamentally enhances its sensitivity. Density functional theory calculations confirm the optimal SAD facilitates dual-site UA adsorption and accelerated charge transfer dynamics. This investigation provides novel insights into the strategic engineering of high-performance SAC-based electrochemical sensors by precisely controlling the atomic-scale structure of active sites.

Introduction

Atomic fabrication technology is a key driver behind the swift advancements in the domain of sensing science.[1] Presently, Single-atom catalysts (SACs) have emerged as a transformative class of catalysts, attributed to their enzyme-mimicking catalytic activities and selectivity.[2] These catalysts distinguish themselves through their maximized atomic efficiency, outstanding efficiency, and sensitivity, positioning them as leading contenders for the development of a diverse array of cost-effective and sustainable sensors with broad applications.[3] SACs are anticipated to demonstrate unprecedented precision in signal amplification for the molecule-scale sensing modes within complex milieus.[4] Notwithstanding their efficacy as an alternative to conventional sensor elements, the rudimentary geometric and electronic structure of SACs, coupled with a scarcity of synergistic active sites, dictates that reaction intermediates necessitate binding to the same site, thereby engendering insurmountable adsorption energy barriers. This limitation has hindered their application in biomolecular sensing.[5] To overcome this bottleneck, the advent of controlled synthetic correlated single-atom catalysts (*c*-SACs) represents a significant breakthrough, showcasing an exceptional capability to surpass the sum of their individual atoms—a design intended to mimic the synergistic dynamics observed in natural enzymes.

Expanding upon the concept of SACs, *c*-SACs refer to an emerging class of catalysts characterized by adjacent yet noncontiguous metal single atom pairs, displaying atomic-level point interactions, unique geometric attributes, and enhanced electrocatalytic performance.[6] Emerging findings suggest that fine-tuning the spatial single-atom distances (SAD) in *c*-SACs does more than modulate individual atomic wavefunctions for refined electronic configurations;[7] when SAD is meticulously tailored to biomolecule interactions, they have the potential to enhance the synergistic effects of adsorbed species,[8] thereby further reshaping reaction pathways and intensify heterogeneous electron

---

[*] B. Jiang, Dr. R. Pan, M. Ji, L. Zhu, Dr. G. Zhang, H. Shi, Dr. K. Yin, Dr. L. Sun
SEU-FEI Nano-Pico Center, Key Lab of MEMS of Ministry of Education, Southeast University, Nanjing 210096, P. R. China
E-mail: yinkuibo@seu.edu.cn
slt@seu.edu.cn

H. Zhang
State Key Laboratory of Digital Medical Engineering, Jiangsu Key Laboratory for Biomaterials and Devices, School of Biological Science and Medical Engineering, Southeast University, Nanjing 210096, P. R. China

J. Liu
Co-Innovation Center of Efficient Processing and Utilization of Forest Resource, School of Materials Science and Engineering, Nanjing Forestry University, Jiangsu, Nanjing, 210037, P. R. China

H. Huang
Department of Materials Science, Fudan University, Shanghai 200433, P. R. China

Dr. S. Wan
College of Optoelectronic Engineering, Chongqing University, Chongqing 400044, P. R. China

transfer mechanisms within the catalytic cycles.[9] This level of tailoring endows sensors with an unmatched capacity to adapt to a variety of target molecules, significantly enhancing the prospects of realizing superior sensitivity and selectivity over existing modalities, and approaching the enzyme-like specific activity. Nonetheless, the most *c*-SACs synthetic methods of achieving a monodisperse intermetal distance and tailoring their spatial proximity to match target molecules present formidable challenges,[10] which has consequently limited research on enhancing the sensing performance of *c*-SACs through the manipulation of SADs. This underscores the pressing need for investigation in the realm of single atom sensing.

Here we evaluated the performance of *c*-SACs in electrochemical sensing with three *c*-SACs with various SADs (9.3 Å, 7.0 Å, and 6.2 Å). Comprehensive characterization confirmed the single-atom dispersion of Ru atom pairs in these *c*-SACs with the predetermined SADs. We then investigated the impact of SADs on the electrocatalytic oxidation of uric acid (UA). The results revealed that when the SAD was reduced to 6.2 Å, the *c*-SACs exhibited the highest UA detection sensitivity (reaching 9.83 $\mu A\,\mu M^{-1}\,cm^{-2}$) and intrinsic activity. Mechanistic studies indicated that the 6.2 Å SAD enabled neighboring Ru sites to cooperatively adsorb the UA molecule, inducing an efficient three-electron oxidation process of UA. Theoretical calculations further corroborated this unique reaction pathway. Further demonstration in portable electrochemical biosensor for sweat UA monitoring illustrated the efficacy and potential of *c*-SACs. This work unveils a new strategy for tuning the SADs to enhance the sensing performance of *c*-SACs, which has important implications for designing highly efficient electrochemical sensors.

Results and Discussion

Materials Synthesis and Characterization

During our experimental studies on various dinuclear Ru N-heterocyclic carbene (NHC) organic complexes as atomic tweezers, [Ru]-benzene with a phenyl backbone while [Ru]-naphthalene with a naphthyl backbone,[7a] we realized that we utilized ligand design strategies to invert [Ru]-benzene moiety within one NHC group, thereby creating the novel complexe, [Ru]-m-benzene, act as an atomic tweezers of further shortening the SAD to 6.2 Å for comparative studies. Following that, Figure 1 illustrates our approach to fabricate the *c*-SACs with SAD between adjacent Ru atoms modulated from 9.3 Å to 7.0 Å, and subsequently to 6.2 Å. The intended catalysts, designated as $Ru_{d=9.3\,Å}$, $Ru_{d=7.0\,Å}$, and $Ru_{d=6.2\,Å}$, were synthesized by immobilizing the aforementioned Ru atomic tweezers onto the carbon nanotubes (CNTs) via π–π stacking interactions between atomic tweezers and CNTs. Additional experimental details can be found in the Supplemental Material.

A comprehensive suite of analytical methods was employed to examine the structural attributes, surface

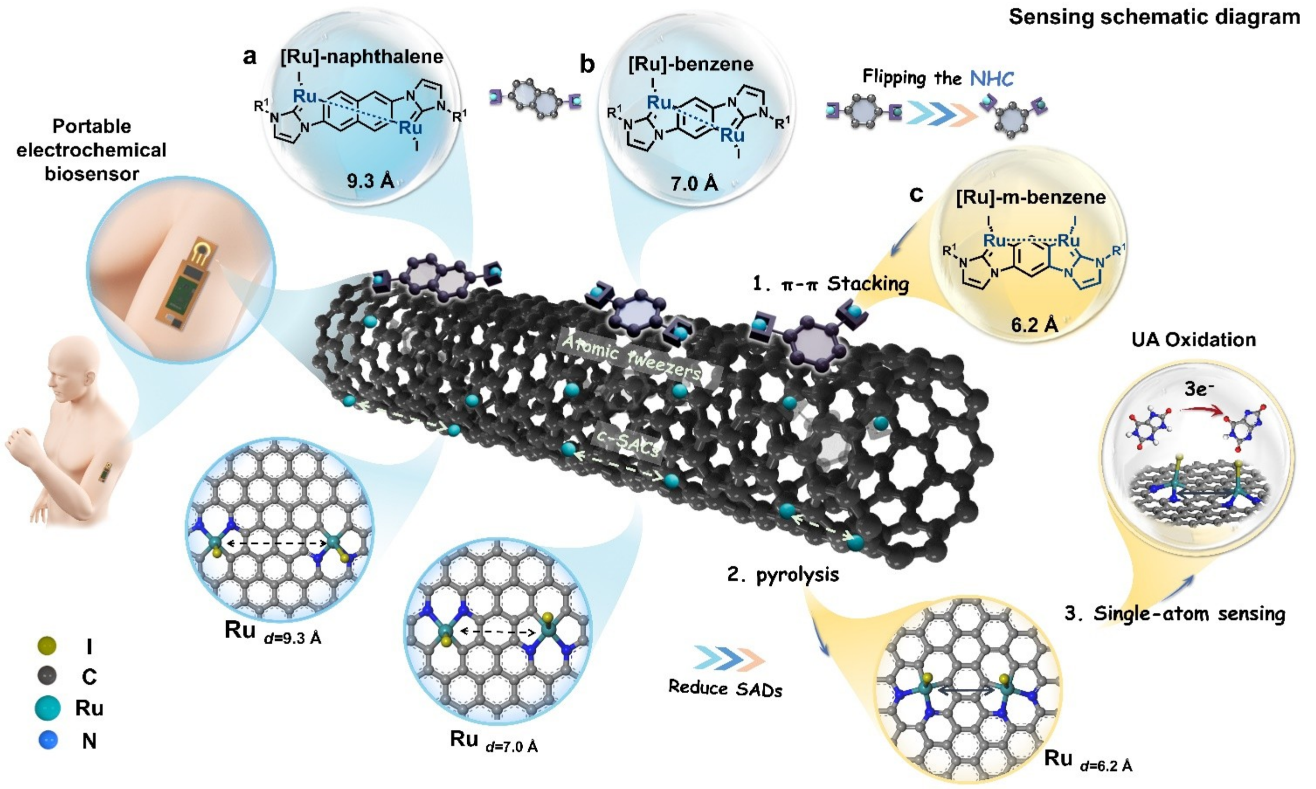

Figure 1. Sensing schematic diagram for the designed Ru based *c*-SACs of (a) $Ru_{d=9.3\,Å}$, (b) $Ru_{d=7.0\,Å}$ and (c) $Ru_{d=6.2\,Å}$, (R^1 = *n*-octyl).

properties, and porosity of the above catalysts. The initial phase of the investigation comprised thermogravimetric analysis (Figure S1) and Raman spectras (Figure S2) of [Ru]-m-benzene, revealing that a fraction of the ligands underwent graphitization while being preserved throughout the calcination process at 550 °C for 3 h under N_2 atmosphere. Moreover, an observed reduction in the intensity ratio of the D-band to G-band (I_D/I_G) was noted from the pristine CNTs to the other samples as seen in Figure S2, suggesting an effective reduction of defects in the CNTs as a result of the calcination process. Additional detail is provided through the measurement of the N_2 adsorption-desorption isotherms (Figure S3) which reveals the presence of mesoporosity as evidenced by the characteristic Type IV isotherms with a pronounced hysteresis loop.[11] The specific surface area, calculated using the Brunauer–Emmett–Teller (BET) method, is found to be 115.2 $m^2 g^{-1}$, providing ample sites for the adsorption of precursors and small molecules. Subsequently, X-ray diffraction (XRD) analysis revealed that all three catalyst samples, along with the CNTs, exhibit two distinct peaks approximately at 24 and 43° (Figure S4), which correspond to the (002) and (100) lattice planes associated with graphitic carbon, respectively. Delving further, transmission electron microscopy (TEM) coupled with elemental mapping analysis (refer to Figures S5,6 and Table S3) was employed to determine the atom dispersal of $Ru_{d=6.2\,Å}$. The analysis revealed a uniform distribution of elemental signatures for Ru, O, N, and I throughout the designated detection area. Moreover, a critical observation from this analysis was the lack of any nanoclusters or nanoparticles. This is consistent with the lack of discernible peaks for Ru aggregation in the XRD pattern.

The use of atomic-resolution Annular dark-field scanning transmission electron microscopy (ADF-STEM) has enabled the detailed visualization and subsequent verification of paired single Ru atoms, and enabled the accurate measurement of interatomic Ru–Ru distances in $Ru_{d=6.2\,Å}$. This technique captures images prominently displaying paired and consistently bright spots, highlighted with yellow rectangles (Figures 2a and b). It is important to note that due to the three-dimensional framework of CNTs, the SADs observed in the images represents projections. Consequently, we employ the median value as an analytical method to ascertain the true SADs. These dual-atom Ru sites of $Ru_{d=6.2\,Å}$ are scattered randomly across the CNTs surface, showing a median distance of 5.6 Å (Figures 2c and S7), notably less than that for $Ru_{d=7.0\,Å}$ and $Ru_{d=9.3\,Å}$ in our previous work.[7a] Meanwhile, such measurements are consistent with the Ru–Ru distances observed in [Ru]-m-benzene according to single-crystal X-ray diffraction analysis (6.2 Å, presented in Figure 2d), confirming the achievement of precise control of the target SAD in $Ru_{d=6.2\,Å}$.

X-ray photoelectron spectroscopy (XPS) is executed to probe the chemical states of surface constituents in each sample. The full scan XPS spectra, exemplified in Figure S8a, reveal the presence of C, O, I, and N elements. In the high-resolution O 1s XPS spectrum, a prominent peak at approximately 532.2 eV is observed, signaling the presence of C–O bonds and thus verifying the retention of oxygen-rich functional groups on the CNTs, which serve to augment the natural hydrophilicity of the Ru catalysts. (Figure S8b). The identification of I $3d_{3/2}$ and I $3d_{5/2}$ peaks in the high-resolution I 3d spectra, shown in Figure S8c, indicates that iodine has been successfully preserved throughout the calcination process.[12] In addition, the N 1s XPS peak is prominently positioned around 398.5–401.1 eV, with specific Binding Energy values of 398.5 eV for pyridinic-N, 399.9 eV for pyrrolic-N, and 401.1 eV for graphitic-N, as illustrated in Figure S8d.[13] Nevertheless, the investigation of Ru 3d signals via XPS is complicated due to the notably low content of ruthenium, with its concentration spanning from 1.36 to 1.62 wt % among the samples, as detailed in Table S4.

To thoroughly investigate the coordination environment and oxidation states of the Ru species in $Ru_{d=9.3\,Å}$, $Ru_{d=7.0\,Å}$, and $Ru_{d=6.2\,Å}$ samples, both X-ray absorption near-edge structure (XANES) and extended X-ray absorption fine structure (EXAFS) measurements were conducted, with the findings showcased in Figures 2e–g. The Ru *K*-edge XANES spectra of Ru in all three samples are similar, with the absorption edge positions for $Ru_{d=9.3\,Å}$, $Ru_{d=7.0\,Å}$, and $Ru_{d=6.2\,Å}$ interspersed between those corresponding to the Ru foil and RuO_2 (Figure 2e), suggesting that Ru species exhibit an average oxidation state intermediary from Ru(0) to Ru(4). The lack of Ru–Ru bonds in Ru catalysts is consistent with the series of characterization findings presented above, and a detail is represented by the solid line in Figure 2f. To precisely ascertain the coordinating atoms around the Ru species, an EXAFS WT analysis was executed (Figure 2g). The quantitatively derived data substantiate the atomic dispersion of Ru species in $Ru_{d=6.2\,Å}$, $Ru_{d=7.0\,Å}$, and $Ru_{d=9.3\,Å}$. In pursuit of a thorough comprehension of the precisely controlled local structure of the catalysts, the EXAFS spectral fitting procedure was conducted (represented by the dotted line in Figure 2f, with details in Table S5). Meanwhile, the EXAFS fittings confirm that all three samples consistently present a uniform coordination motif, wherein each Ru atom is coordinated by two N atoms and one I atom. This finding suggests that the coordination environments characteristic of Ru in [Ru]-benzene, [Ru]-naphthalene, and [Ru]-m-benzene complexes are preserved post-calcination.

Electrochemical Responses of Ru c-SACs Towards UA Oxidation

The electrocatalytic activity of the $Ru_{d=6.2\,Å}$, $Ru_{d=7.0\,Å}$, and $Ru_{d=9.3\,Å}$ toward the UA oxidation was evaluated using a three-electrode configuration in Phosphate buffer saline (PBS, 0.1 M, pH = 7.4). The differential pulse voltammetry (DPV) curves are recorded at varying concentrations of 0 to 200 μM of UA to evaluate all samples the electrochemical response (Figures 3a and S9). Our findings reveal that the doping of single-atom Ru significantly enhances the electrochemical sensing performances of CNTs for UA. As the SAD decreases, we observed that the sensing performance of $Ru_{d=7.0\,Å}$ and $Ru_{d=9.3\,Å}$ remains relatively comparable. Notably, a further decrease in SAD to 6.2 Å leads to a

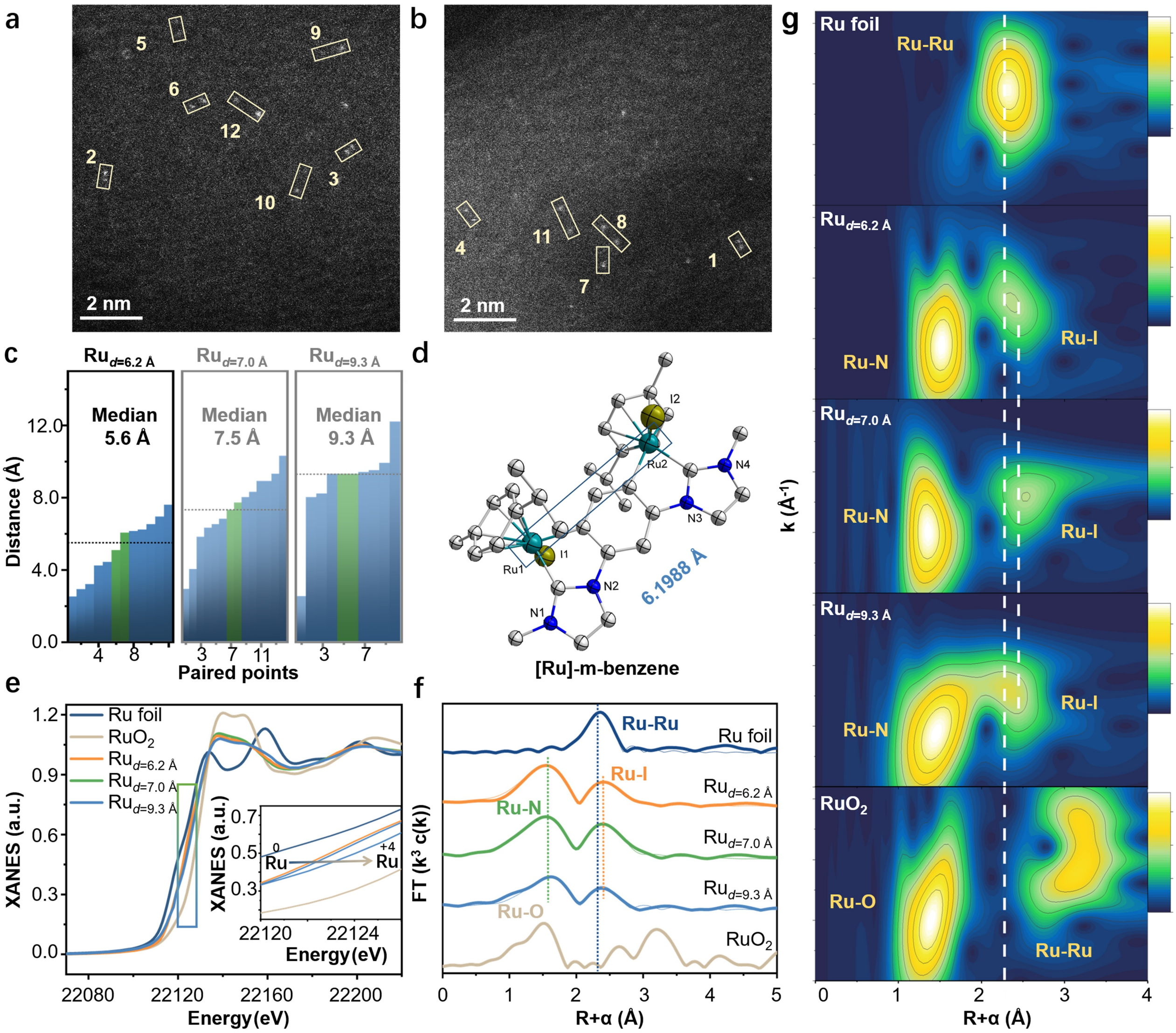

Figure 2. (a, b) Atomic-resolution ADF-STEM images. (c) Comparison of inter-distance distribution. (d) The molecular structures of [Ru]-m-benzene.[15] (e) XANES spectra, (f) the solid line represents Fourier transformed k^3-weighted χ(k)-function of the EXAFS spectra for Ru K-edge of Ru foil, RuO_2, $Ru_{d=9.3 Å}$, $Ru_{d=7.0 Å}$, and $Ru_{d=6.2 Å}$, the dashed line represents the R spaces fitting curves, and (g) the corresponding wavelet transform (WT) plots for k^3-weighted Ru K-edge EXAFS signal.

significant enhancement in performance (Figure 3b). The sensitivity of $Ru_{d=6.2 Å}$ is determined to be an impressive 9.83 μA μM^{-1}cm^{-2}, demonstrating a consistent linear response over the concentration range from 0.05 to 140 μM, and its sensitivity is 2.35-fold and 2.62-fold higher than that of $Ru_{d=7.0 Å}$ (4.18 μA μM^{-1}cm^{-2}) and $Ru_{d=9.3 Å}$ (3.74 μA μM^{-1}cm^{-2}), respectively (Figure 3c). This performance was superior to most of the previously reported electrochemistry biosensors (refer to Table S6).[14] Additionally, the limits of detection (LODs, $3S_a/b$, where S_a represents the standard deviation of the 11-blank sample response and b corresponds to the slope of the calibration curve) are calculated to be 2.38 μM for $Ru_{d=6.2 Å}$, 5.89 μM for $Ru_{d=7.0 Å}$ and 8.45 μM for $Ru_{d=9.3 Å}$, demonstrating a superior detection capability at the 6.2 Å SAD.

Moreover, there is a well-established direct correlation between the double-layer capacitance (C_{dl}) and the electrochemically active surface areas (ECSA).[16] To ascertain the C_{dl} values, cyclic voltammetry (CV) experiments were performed outside the Faraday regions, as shown in Figure S10. The calculated ECSA values for the $Ru_{d=6.2 Å}$, $Ru_{d=7.0 Å}$, and $Ru_{d=9.3 Å}$ are determined to be 55.12, 51.38, and 43.28 mF cm^{-2}, respectively (Figure S10d). Normalization of DPV peak currents to both Ru mass and ECSA allows for an insightful comparison of the intrinsic catalytic activity at individual Ru sites. Upon this normalization, the data indicate that $Ru_{d=6.2 Å}$ exhibits exceptionally high catalytic activity, with values of 141.9 mg mA^{-1} and 1.26 μA cm^{-2} (Figure 3d). These values are significantly greater than those recorded for $Ru_{d=7.0 Å}$ and $Ru_{d=9.3 Å}$,

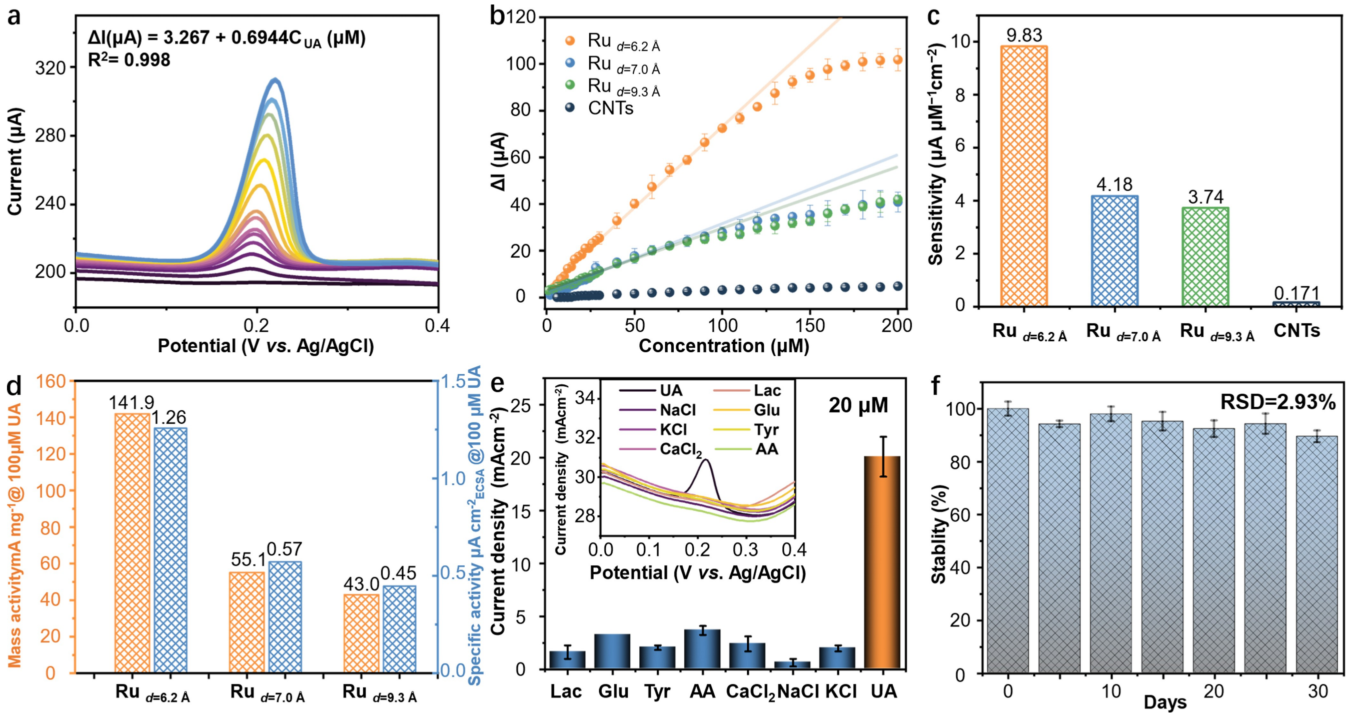

Figure 3. (a) DPV recorded at varying concentrations of UA for Ru$_{d=6.2\,Å}$. (b) Summary curve corresponding to the DPV peak current and (c) sensitivity of Ru catalysts and CNTs. (d) the DPV peak current for detection of 100 μM UA according to Ru mass and ECSA normalization. (e) Selectivity (Lactic acid, Lac; glucose, Glu; tyrosine, Tyr; ascorbic acid, AA) and f) stability of Ru$_{d=6.2\,Å}$. The error bars correspond to standard deviation obtained from five measurements ($n=5$).

highlighting the superior performance with the reduced SAD.

Assessing the selectivity and stability of catalysts is paramount owing to the complexity and diversity of biological environments. As shown in Figure 3e, the introduction of various substances elicited negligible oxidation peaks, indicating that Ru$_{d=6.2\,Å}$ possesses excellent selectivity. Furthermore, the long-term stability of Ru$_{d=6.2\,Å}$ was examined through DPV curves. The outcomes demonstrate that Ru$_{d=6.2\,Å}$ maintains excellent long-term stability towards UA. Impressively, after 30 days of storage, Ru$_{d=6.2\,Å}$ retains at least 89.5 % of its initial activity, with a relative standard deviation (RSD) of 2.93 % (Figure 3f and S11).

Insights into SAD-Determined UA Oxidation Kinetics Relation and Mechanism

To explore the mechanism for enhanced UA oxidation performance through regulation of SADs, we initially investigated the influence of solution pH value on their oxidation currents and peak potentials (E_{pa}), attributing to the involvement of protons in the UA electrochemical oxidation processes (Figures 4a–c).[17] As shown in Figure 4b, it is observed that their E_{pa} shift negatively with increasing pH values, with the slopes of −62, −57, and −61 mV pH^{-1} for Ru$_{d=6.2\,Å}$, Ru$_{d=7.0\,Å}$, and Ru$_{d=9.3\,Å}$ within the range of 4.0–9.0. The ratio of transferred proton number (m) and transferred electron number (n) can be expressed with the following equation:[18]

$$\frac{dE_{pa}}{dpH} = 2.303\frac{mRT}{nF} \qquad (1)$$

Where R is the gas constant (R = 8.314 J mol^{-1} K^{-1}), T is the absolute temperature (T = 298 K), and F is the Faraday constant (F = 96485 C mol^{-1}). The calculated values of m/n are 1.05, 0.96, and 1.03 for the above catalyst, indicating an equivalent count of protons and electrons involved in the UA oxidation reaction. Simultaneously, the peak current reaches its maximum at approximately pH 6 and subsequently decreases as pH increases (Figure 4c). We speculate that at elevated pH values, an excess of –OH might adsorb and block the active sites of Ru, leading to a reduction in peak current. In contrast, at decreased pH values, a higher concentration of protons could impact the balance of UA dehydrogenation oxidation.

Furthermore, the impact of scan rate on the electrochemical signals of UA was investigated for Ru$_{d=6.2\,Å}$, Ru$_{d=7.0\,Å}$, and Ru$_{d=9.3\,Å}$ (Figures 4d and S12a–c). For the totally irreversible electrochemical oxidation process of UA, the linear relationship between E_{pa} and the logarithm of scan rate ($\log v$) could be described by the Laviron's equation:[18b,19]

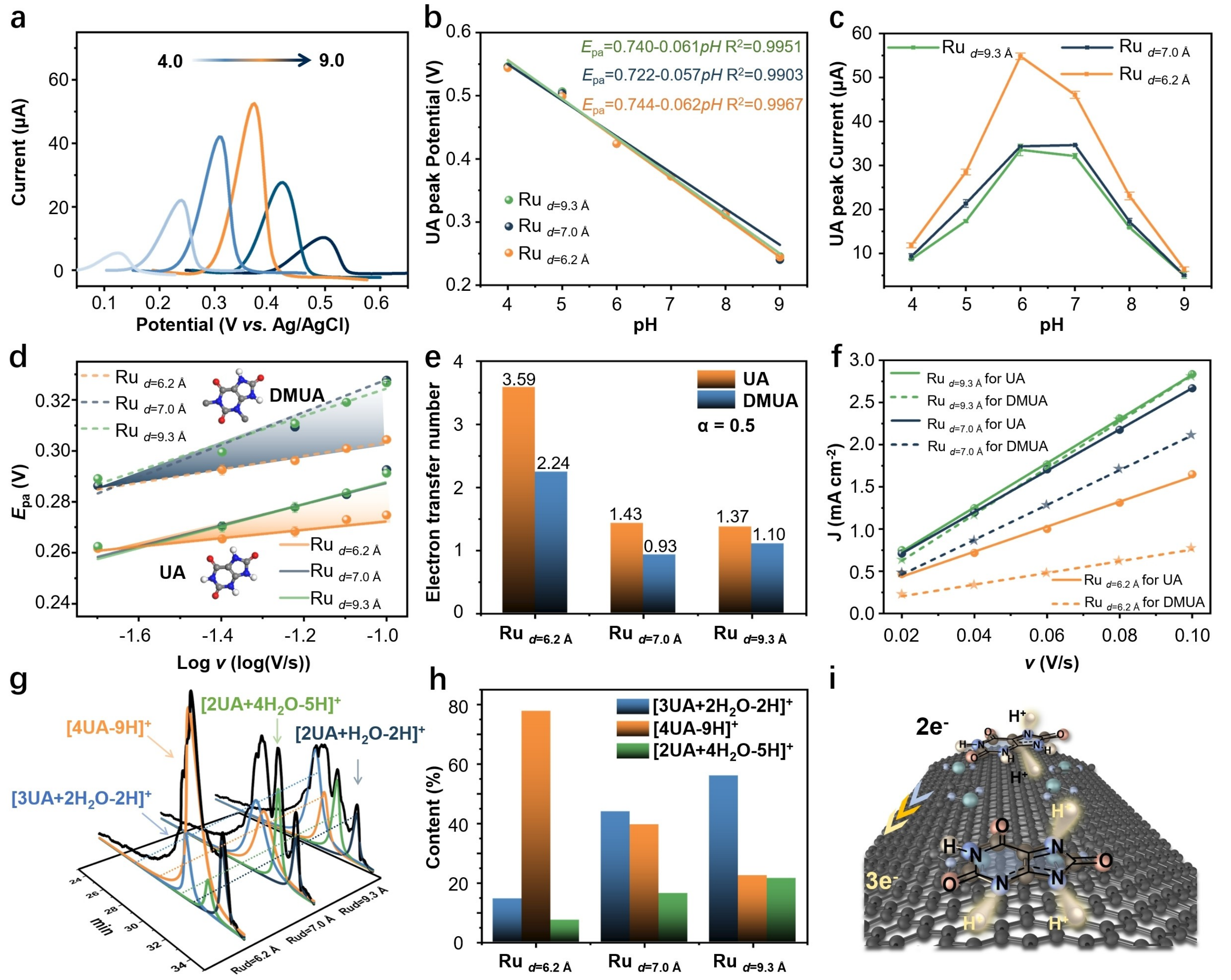

Figure 4. (a) DPV curves of the $\mathrm{Ru}_{d=6.2\,\text{Å}}$ in 100 μM UA at different pH values. (b) Relationship of the UA oxidation peak potential and (c) current vs. pH value, the error bars correspond to standard deviation obtained from five measurements ($n=3$). (d) The plots of peak potential versus the logarithm of the scanning speed. (e) The number of electrons transferred determined by the Laviron equation. (f) Plot of peak current density versus the scan rate. (g) HPLC chromatograms of UA oxidation reaction solutions catalyzed by different Ru catalysts and (h) the relative content of the reaction products. (i) Schematic illustration of the Ru catalyst for the UA oxidation.

$$E_{\mathrm{pa}} = \mathrm{E}^0 + \frac{2.303\mathrm{RT}\log v}{(1-\alpha)\mathrm{nF}} \tag{2}$$

Where E^0 stands for standard potential, v stands for scan rate and the α is interconnected to a coefficient of charge transfer, with α set as 0.5 in a completely irreversible electrochemical process.[18a,20] Therefore, we can calculate the transferred electron number n as 3.59, 1.43, and 1.37 (Figure 4e), indicating that when SAD equals 6.2 Å, a potential novel transfer process occurs. While in other cases, it follows a typical two-electron two-proton transfer process.[17,21] The Nyquist plots revealed a significant divergence in the low-frequency region between $\mathrm{Ru}_{d=6.2\,\text{Å}}$ and the other two catalysts, indicating that $\mathrm{Ru}_{d=6.2\,\text{Å}}$ might follow a distinct reaction mechanism (Figure S13). To further validate its electron transfer number, we performed the same tests on 1,3-Dimethyluric acid (DMUA) by selectively substituting methyl groups at two potential deprotonation sites. We found that for $\mathrm{Ru}_{d=6.2\,\text{Å}}$, the transferred electron number n significantly decreased from 3.59 to 2.24, while the changes for $\mathrm{Ru}_{d=7.0\,\text{Å}}$, and $\mathrm{Ru}_{d=9.3\,\text{Å}}$ were not significant. This suggests the possible existence of a distinctive three-electron transfer mechanism. Furthermore, Figure 4f depicts a clear linear correlation between the scan rate and the resultant anodic peak current, confirming the surface-controlled electrochemical process of both UA and DMUA on the electrode surface.[22]

HPLC-MS analysis was performed to further investigate the underlying mechanism. As illustrated in the Figure 4g, the retention times of the oxidation products were 30.8, 31.4, 32.5, and 33.6 min, each characterized by parent ions with m/z values of 536.07, 663.04, 403.06, and 352.05, respectively (Figure S14). Subsequently, we determined their specific charge formula were $[3\mathrm{UA}+2\mathrm{H_2O}\text{-}2\mathrm{H}]^+$ (speculated to be a two-electron transfer product, $\mathrm{UA_1}^{2+}$), $[4\mathrm{UA}\text{-}9\mathrm{H}]^+$ (a three-electron transfer product, UA^{3+}), $[2\mathrm{UA}+4\mathrm{H_2O}\text{-}5\mathrm{H}]$ (the other two-electron transfer product, UA_2^{2+}), and [2UA + H_2O-2H]$^+$ (product UA^+), respectively. Additionally, we used the product UA^+ to semi-quantitatively analyze the product concentrations (Figure 4h) and observed that the content of the three-electron product UA^{3+} was the highest at a SAD of 6.2 Å. This concentration progressively diminished with a decrease in SAD. Conversely, the concentrations of the two-electron products UA_1^{2+} and UA_2^{2+} displayed an inverse relationship, increasing as the SAD expanded. These findings suggest that with SADs of 7.0 Å and 9.3 Å, the oxidation of UA tends to predominantly involve two-electron transfers. In contrast, at a SAD of 6.2 Å, the three-electron transfer process is favored in the oxidation of UA (Figure 4i). We subsequently employ the Randles–Sevcik equation[23] to scrutinize the correlation between transferred electron number n and oxidation peak currents (I_{pa}):

$$I_{Pa} = 2.69 \times 10^5 A D^{\frac{1}{2}} n^{\frac{3}{2}} v^{\frac{1}{2}} C \tag{3}$$

where A, D, and C are ECSA, diffusion coefficient and bulk concentration of UA, respectively. An increase in the value of n increases from 2 to 3, a significant 183 % increase in I_{pa} is observed, remaining consistent with the previously mentioned changes in sensitivity and catalytic activity.

Theoretical Calculation

Density functional theory (DFT) calculations were performed to verify the catalytic mechanism of three-electron transfer in UA oxidation over SAD. Initially, we calculated the overall d-band center for the model, identifying a negative correlation between the SAD and the d-band center (Figure S15), which is consistent with reports from previous literature.[7a] Then, we calculated the adsorption energy (ΔE_{ad}) of UA adsorbed on the Ru catalysts with varying SAD. As shown in Figure 4f, there is a pronounced decrease in capacitive behavior for $Ru_{d=6.2\,Å}$, despite the similarity in both Ru mass and ECSA, which signifies the adsorption characteristics for UA (or DMUA). This attenuated capacitive activity can likely be traced back to the unique SAD of 6.2 Å, which feasibly facilitates the simultaneous adsorption of two oxygen atoms by a pair of Ru atoms on one solitary UA. This scenario that each Ru atom engages with a single oxygen atom from UA molecules when the SAD widens to 7.0 Å or 9.3 Å. Based on these findings, we conducted the calculations on all potential adsorption interactions where the single Ru atom bonds with different oxygen atoms on UA (refer to Figure S16 for details). When compared with $Ru_{d=7.0\,Å}$ (−1.53 eV) and $Ru_{d=9.3\,Å}$ (−1.32 eV), $Ru_{d=6.2\,Å}$ demonstrated the favorable ΔE_{ad} of −2.51 eV.

Subsequently, we calculated the pKa values[24] for the hydrogen atoms in different positions on the UA molecule and discover that the proton at position 1 exhibits a pKa of 7.25, which is distinctly lower than those at position 2 (15.6) and position 3 (12.6) shown in Figure S17. Under identical structural conditions, a lower pKa indicates a greater propensity to donate protons.[24a,25] Hence, we postulate that the hydrogen at position 1 is most likely to be removed first, yielding the intermediate product UA^+. Following this, we proceeded to predict the pKa values for the hydrogens at positions 2 and 3 of UA^+, finding them to be 8.24 and 8.04 respectively, indicating that their oxidizability is quite similar. Consequently, we propose a more plausible three-electron transfer pathway for UA oxidation, as illustrated in Figure S18. The oxidation of UA initially involves the removal of the hydrogen at position 1, followed by the subsequent oxidation and removal of either the hydrogen at position 2 or position 3. We define the pathway that involves the removal of hydrogen at the pyran ring at position 2 as pathway 1. Conversely, the removal of hydrogen at the hexagonal ring from position 3 is defined as pathway 2. Eventually, the final hydrogen is removed, completing the three-electron oxidation process of UA. As shown in Figures 5a–c, we also calculate the Gibbs free energies of intermediates ($* + C_5O_3N_4H_4 \rightarrow *C_5O_3N_4H_3 \rightarrow *C_5O_3N_4H_2 \rightarrow *C_5O_3N_4H_1$) for $Ru_{d=6.2\,Å}$, $Ru_{d=7.0\,Å}$, and $Ru_{d=9.3\,Å}$ with different SADs (Blue represents Pathway 1 while green signifies Pathway 2). All calculated pathways indicate that when the interatomic distance is 6.2 Å, the occurrence of dual-site adsorption leads to a lower overall reaction barrier, favoring a three-electron transfer dehydrogenation reaction. In contrast, for $Ru_{d=7.0\,Å}$, and $Ru_{d=9.3\,Å}$, where single-site adsorption occurs, the significantly higher energy barriers make the three-electron transfer dehydrogenation reaction less likely. This explains why $Ru_{d=6.2\,Å}$ exhibits the most exceptional catalytic performance, consistent with experimental outcomes.

Figures 5d–e show the charge density images of the UA molecule under varying SAD conditions, with a particular focus on the hydrogen atoms at positions 2 and 3 of the UA molecule. It can be observed the hydrogen atoms at positions 2 and 3 for $Ru_{d=6.2\,Å}$ exhibit a more pronounced electrophilic deficiency compared to those at $Ru_{d=7.0\,Å}$, and $Ru_{d=9.3\,Å}$. This enhanced electron deficiency character facilitates the occurrence of the dehydrogenation oxidation reaction. Overall, the $Ru_{d=6.2\,Å}$ exhibits a superior electrochemical sensing sensitivity, attributed to its optimal SAD that facilitates a three-electron transfer mechanism effectively matching with the UA molecule.

Practical In Situ Electrochemical UA Identification in Sweat

The detection of UA in sweat is pivotal for the early identification of diseases such as gout and metabolic disorders, and delivering more comprehensive insights for personalized healthcare.[26] The $Ru_{d=6.2\,Å}$ exhibits superior electrocatalytic performance for the electro-oxidation of UA. As a demonstration shown in Figure 6a, we utilized a polyimide (PI) substrate material integrated with wireless components to assemble a flexible, highly sensitive, and real-time electrochemical biosensor for the non-invasive in situ UA identification in sweat. The $Ru_{d=6.2\,Å}$ was employed as the working electrode (WE), with Au and Ag/AgCl serving as the counter electrode (CE) and reference

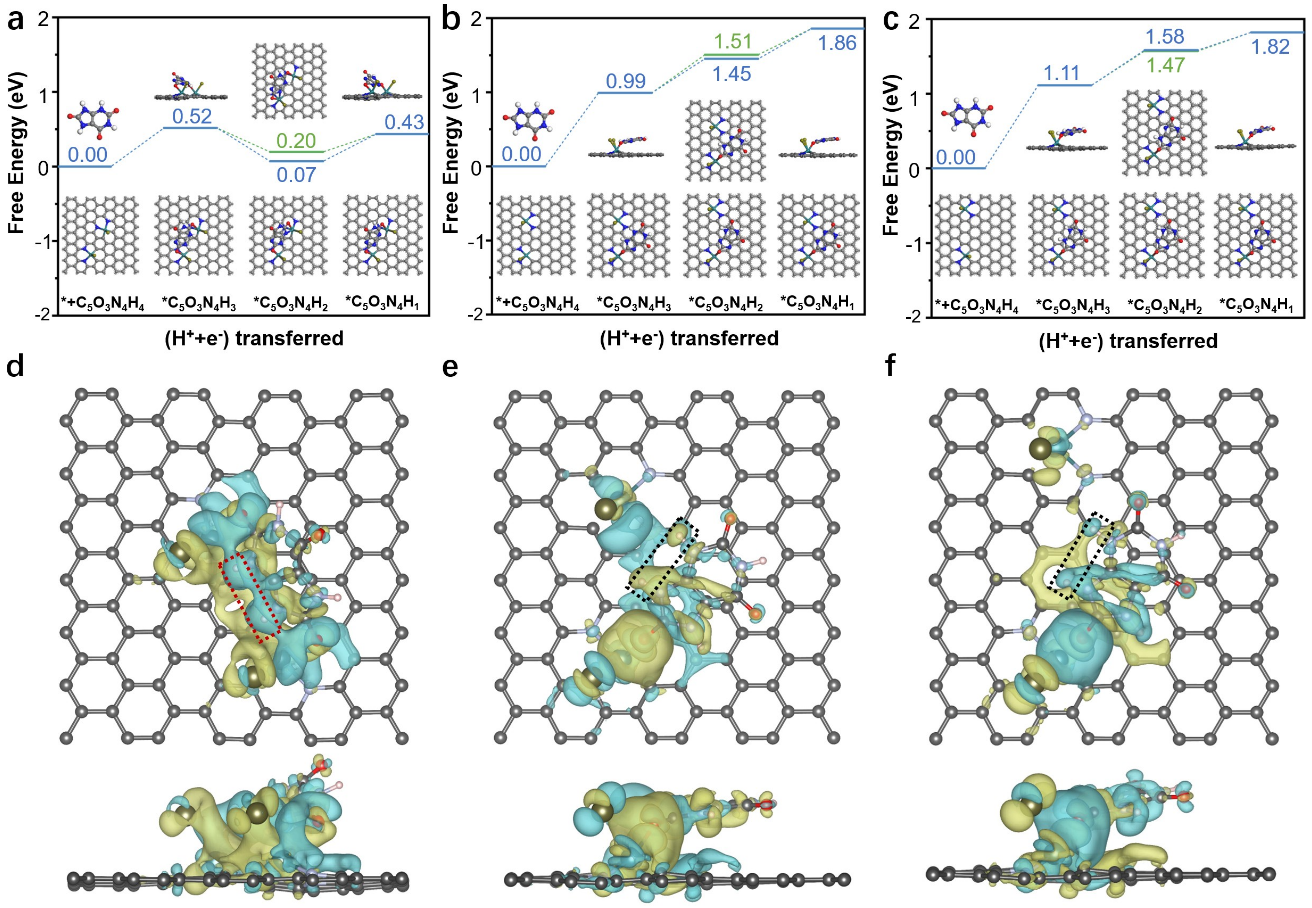

Figure 5. Gibbs free-energy diagram of UA electrooxidation pathway on (a) Ru$_{d=6.2\,Å}$, (b) Ru$_{d=7.0\,Å}$ and (c) Ru$_{d=9.3\,Å}$ (the inset shows the side views of adsorption systems on the Ru catalysts. blue, pathway 1; green, pathway 2). The differential charge density of the UA electrooxidation of (d) Ru$_{d=6.2\,Å}$, (e) Ru$_{d=7.0\,Å}$ and (f) Ru$_{d=9.3\,Å}$. (The yellow and blue regions indicate the accumulation and depletion of electrons, respectively).

electrode (RE), respectively (Figure S19a). Sweat sampling utilizing a polydimethylsiloxane (PDMS) microfluidic chip ensured tight integration with the skin and sensor.[27] Additionally, a droplet of blue liquid was introduced at the inlet and visually monitored for fluid flow (Figure 6a). The entire chamber filled rapidly with the blue liquid within 90 seconds, with no leakage observed, demonstrating the chip‘s capacity for effective sweat enrichment. Through the microfluidic chip, the UA within sweat will generate a distinct DPV response from Ru$_{d=6.2\,Å}$ at the gold electrode coated on the screen-printed electrodes. The electrochemical sensor, in conjunction with a bespoke app, enables the visualization of the detection current directly on a smartphone interface. The communication between the microcontroller unit (MCU) and the MS02 biosensor chip is enabled through the I2C protocol, with the MCU commandeering the initiation of measurements. The harvested current signals from the three-electrode array are conveyed to the MS02, where a Transimpedance Amplifier transmutes these currents into voltage readings for the MCU's consideration. This voltage data is then processed by the MCU and wirelessly relayed to the end-user's device via 2.4 GHz Bluetooth for graphing and further analysis, as shown in Figure 6b. The detector is comprised of a microcontroller, Bluetooth connectivity, and a power supply, which are detailed in Figure 6c and Figure S19b.

Additionally, linear detection experiments performed in artificial sweat generated a linear regression formula of $I(\mu A) = 1.121 + 0.0661 \times C_{UA}(\mu M)$, as depicted in Figure 6d. Ultimately, we conducted real sweat detection on 7 healthy volunteers after exercise, revealing a positive correlation with results from standard colorimetric assays, corroborating the device‘s practicality on-site and real-time monitoring (Figure 6e).

Conclusion

In summary, three Ru-based *c*-SACs were designed and developed with SADs decreasing consecutively from 9.3 Å to 7.0 Å, and further to 6.2 Å, and Ru SAD was crucial for the electrochemical oxidation of UA. The sensitivity of Ru$_{d=6.2\,Å}$ is determined to be an impressive 9.83 $\mu A\,\mu M^{-1} cm^{-2}$ for UA detection. Our kinetic studies and product examination uncover that the outstanding performance of Ru$_{d=6.2\,Å}$ is due to its unique ability to promote a three-electron transfer mechanism throughout the UA oxidation process. For supporting these experimental results,

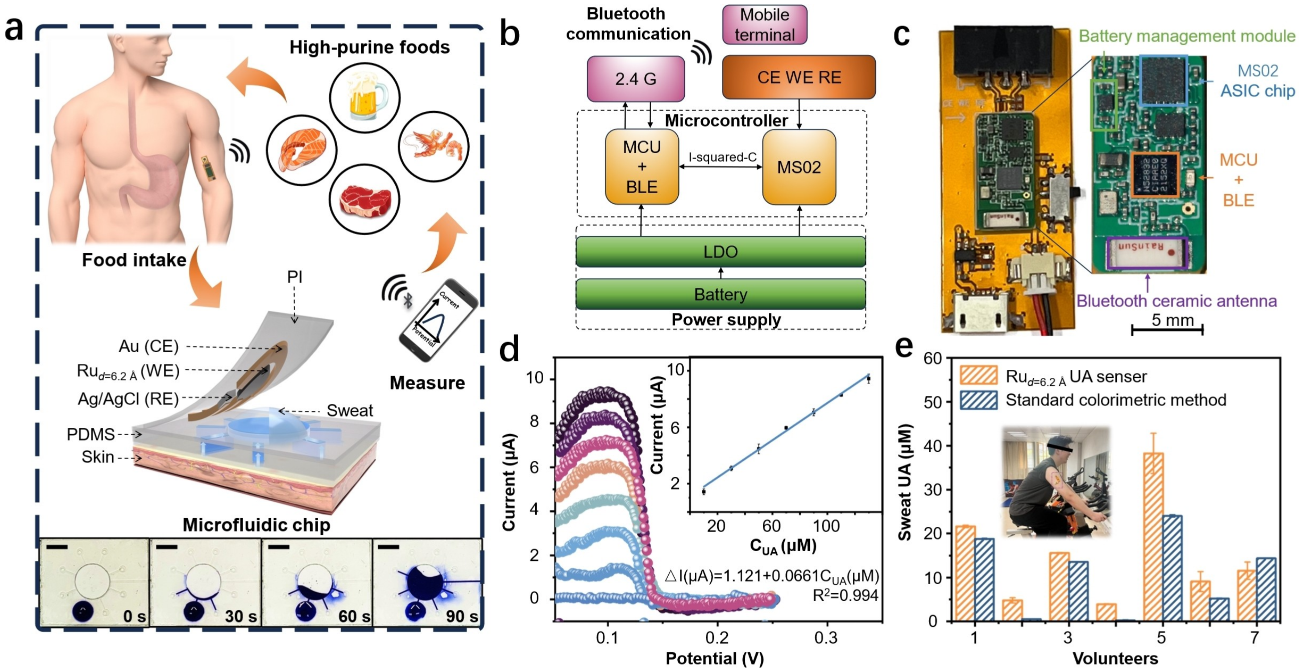

Figure 6. (a) Schematic illustration of portable electrochemical device and the microfluidic chip. Scale bars, 5 mm. (b) System-level block diagram of signal conversion, processing, and wireless transmission. (c) Photographs of the wearable physical device (Bluetooth Low Energy, BLE). (d) DPV curves of the electrochemical system toward target UA standards with different concentrations in artificial sweat with pH = 6.5 (inset: calibration plots between the current and the UA concentration). (e) The detection of UA in real sweat under the different volunteers of the UA flexible sensor and the detection result based on a commercial standard UA colorimtric method. The error bars represent the standard deviations of the peak amplitude measured from 3 cycles.

DFT calculations highlight that the enhanced three-electron transfer is a direct consequence of the optimal SAD, the 6.2 Å SAD allows beneficial dual-site adsorption and accelerated charge transfer dynamics between the UA molecule and adjacent Ru active sites. Additionally, the Ru$_{d=6.2\,Å}$ catalyst was integrated into a flexible, portable electrochemical biosensor for the real-time determination of UA levels in human sweat. This insightful study lays a foundational framework for the tailored design of high-performance single-atom catalyst sensor through the precision-tuning of SADs.

Supporting Information

The authors have cited additional references within the Supporting Information.[28]

Acknowledgements

This work was supported by the National Key Research and Development Program of China (2024YFA1207900), the National Natural Science Foundation of China (No. 12174050 and T2321002), the Natural Science Foundation of Jiangsu Province (BK20231411), the new cornerstone science foundation and XPLORER PRIZE, the Postgraduate Research & Practice Innovation Program of Jiangsu Province (KYCX24_0500), and the Fundamental Research Funds for the Central Universities. We gratefully acknowledge HZWTECH for providing computation facilities.

Conflict of Interest

The authors declare that they have no known competing financial interests or personal relationships that could have appeared to influence the work reported in this paper.

Data Availability Statement

The data that support the findings of this study are available from the corresponding author upon reasonable request.

Keywords: three-electron transfer · UA sensing · single-atomic inter-distance · sweat detection · correlated single-atom catalysts

---

[1] a) T. Esat, D. Borodin, J. Oh, A. J. Heinrich, F. S. Tautz, Y. Bae, R. Temirov, *Nat. Nanotechnol.* **2024**, *19*, 1466–1471; b) Y. Ding, C. Wang, M. Zeng, L. Fu, *Adv. Mater.* **2023**, *35*, 2306689; c) O. Dyck, M. Ziatdinov, D. B. Lingerfelt, R. R. Unocic, B. M. Hudak, A. R. Lupini, S. Jesse, S. V. Kalinin, *Nat. Rev. Mater.* **2019**, *4*, 497–507.

[2] a) L. Mao, *ACS Sens.* **2024**, *9*, 1620–1621; b) M. Pumera, P. Thakkar, *TrAC Trends Anal. Chem.* **2024**, *174*, 117660; c) T.

Chu, C. Rong, L. Zhou, X. Mao, B. Zhang, F. Xuan, *Adv. Mater.* **2023**, *35*, e2206783; d) Y. Shu, Q. Mo, Q. Gao, *ChemCatChem* **2024**, *16*, e202301634.

[3] a) R. Li, W. Guo, Z. Zhu, Y. Zhai, G. Wang, Z. Liu, L. Jiao, C. Zhu, X. Lu, *Anal. Chem.* **2023**, *95*, 7195–7201; b) X. Li, X. I. Pereira-Hernandez, Y. Chen, J. Xu, J. Zhao, C. W. Pao, C. Y. Fang, J. Zeng, Y. Wang, B. C. Gates, J. Liu, *Nature* **2022**, *611*, 284–288; c) L. Jiao, W. Xu, Y. Wu, H. Yan, W. Gu, D. Du, Y. Lin, C. Zhu, *Chem. Soc. Rev.* **2021**, *50*, 750–765; d) Y. Zhang, S. Ni, C. Chong, J. Xu, X. Mu, X.-D. Zhang, *Appl. Mater. Today* **2021**, *23*, 101029; e) M. Zhou, Y. Jiang, G. Wang, W. Wu, W. Chen, P. Yu, Y. Lin, J. Mao, L. Mao, *Nat. Commun.* **2020**, *11*, 3188.

[4] a) X. Gao, H. Wei, W. Ma, W. Wu, W. Ji, J. Mao, P. Yu, L. Mao, *Nat. Commun.* **2024**, *15*, 7915; b) X. Zhang, P. Chen, S. He, B. Jiang, Y. Wang, Y. Cheng, J. Peng, F. Verpoort, J. Wang, Z. Kou, *InfoMat* **2023**, *5*, e12421; c) A. B. Taylor, P. Zijlstra, *ACS Sens.* **2017**, *2*, 1103–1122.

[5] a) X. Yang, L. Xu, Y. Li, *Coord. Chem. Rev.* **2024**, *516*, 215961; b) L. Liu, A. Corma, *Chem. Rev.* **2018**, *118*, 4981–5079.

[6] a) J. Shan, C. Ye, Y. Jiang, M. Jaroniec, Y. Zheng, S. Qiao, *Sci. Adv.* **2022**, *8*, eabo0762; b) C. Chu, D. Huang, S. Gupta, S. Weon, J. Niu, E. Stavitski, C. Muhich, J. H. Kim, *Nat. Commun.* **2021**, *12*, 5179; c) Z. Jin, P. Li, Y. Meng, Z. Fang, D. Xiao, G. Yu, *Nat. Catal.* **2021**, *4*, 615–622.

[7] a) B. Jiang, J. Zhu, Z. Xia, J. Lyu, X. Li, L. Zheng, C. Chen, S. Chaemchuen, T. Bu, F. Verpoort, S. Mu, J. Wu, J. Wang, Z. Kou, *Adv. Mater.* **2024**, *36*, 2310699; b) Y. Hu, L. Dai, B. Li, Z. Li, *Adv. Sustainable Syst.* **2024**, *8*, 2300564; c) I. Khivrich, S. Ilani, *Nat. Commun.* **2020**, *11*, 2299; d) A. Vainchtein, Y. Starosvetsky, J. D. Wright, R. Perline, *Phys. Rev. E* **2016**, *93*, 042210.

[8] a) S. Jiang, J. Xue, T. Liu, H. Huang, A. Xu, D. Liu, Q. Luo, J. Bao, X. Liu, T. Ding, Z. Jiang, T. Yao, *J. Am. Chem. Soc.* **2024**, *146*, 29084–29093; b) H. Jin, R. Zhao, P. Cui, X. Liu, J. Yan, X. Yu, D. Ma, W. Song, C. Cao, *J. Am. Chem. Soc.* **2023**, *145*, 12023–12032; c) X. Huang, B. Xu, J. Feng, S. Hu, W. Dou, T. Yang, C. Zhan, S. Liu, Y. Ji, Y. Li, C. W. Pao, Z. Hu, Q. Shao, X. Huang, *J. Am. Chem. Soc.* **2023**, *145*, 28010–28021.

[9] a) B. Tang, Y. Zhou, Q. Ji, Z. Zhuang, L. Zhang, C. Wang, H. Hu, H. Wang, B. Mei, F. Song, S. Yang, B. M. Weckhuysen, H. Tan, D. Wang, W. Yan, *Nat. Synth.* **2024**, *3*, 878–890; b) X. Hai, Y. Zheng, Q. Yu, N. Guo, S. Xi, X. Zhao, S. Mitchell, X. Luo, V. Tulus, M. Wang, X. Sheng, L. Ren, X. Long, J. Li, P. He, H. Lin, Y. Cui, X. Peng, J. Shi, J. Wu, C. Zhang, R. Zou, G. Guillen-Gosalbez, J. Perez-Ramirez, M. J. Koh, Y. Zhu, J. Li, J. Lu, *Nature* **2023**, *622*, 754–760.

[10] a) Y. Huang, J. Xiong, Z. Zou, Z. Chen, *Adv. Mater.* **2024**, e2312182; b) Y. Chen, J. Lin, Q. Pan, X. Liu, T. Ma, X. Wang, *Angew. Chem. Int. Ed.* **2023**, *62*, e202306469.

[11] F. Gao, F. Wu, X. Zhang, B. Jiang, Q. Li, *J. Inorg. Organomet. Polym. Mater.* **2023**, *33*, 328–336.

[12] W. Qu, J. Zhu, G. Cao, S. Chen, Y. Tan, B. Chen, M. Zhang, *Small* **2024**, *20*, 2310475.

[13] a) J. Wang, L. Chen, H. Zhao, P. Kumar, S. R. Larter, M. G. Kibria, J. Hu, *ACS Catal.* **2023**, *13*, 2637; b) C. Chen, Z. Wang, Y. Gong, J. Wang, Y. Yuan, H. Cheng, W. Sang, S. Chaemchuen, F. Verpoort, *Carbon* **2021**, *174*, 284.

[14] a) Y. Liu, Y. Zhang, C. Wang, X. Zeng, J. Lei, J. Hou, D. Huo, C. Hou, *ACS Appl. Nano Mater.* **2024**, *7*, 6273–6283; b) Z. Qin, B. Tang, G. Zhang, C. Zhu, K. Jiang, B. Zhang, F.-Z. Xuan, *Nano Res.* **2024**, *17*, 7658–7664; c) Y. Liu, P. Zhao, Y. Liang, Y. Chen, J. Pu, J. Wu, Y. Yang, Y. Ma, Z. Huang, H. Luo, D. Huo, C. Hou, *Talanta* **2023**, *254*, 124171; d) Y. Zhang, C. Hou, P. Zhao, X. Zeng, Y. Liu, J. Chen, Y. Gao, C. Wang, J. Hou, D. Huo, *ACS Appl. Mater. Interfaces* **2023**, *15*, 43541–43549; e) R. Zeng, L. Lin, H. Gong, Y. Li, J. Xu, L. Huang, W. Wang, S. Lin, D. Tang, S. Guo, *Chem Catal.* **2023**, *3*, 100514; f) N. Wu, H. Zhong, Y. Zhang, X. Wei, L. Jiao, Z. Wu, J. Huang, H. Wang, S. P. Beckman, W. Gu, C. Zhu, *Biosens. Bioelectron.* **2022**, *216*, 114609; g) X. Xie, D. P. Wang, C. Guo, Y. Liu, Q. Rao, F. Lou, Q. Li, Y. Dong, Q. Li, H. B. Yang, F. X. Hu, *Anal. Chem.* **2021**, *93*, 4916–4923; h) F. X. Hu, T. Hu, S. Chen, D. Wang, Q. Rao, Y. Liu, F. Dai, C. Guo, H. B. Yang, C. M. Li, *Nano-Micro Lett.* **2020**, *13*, 7.

[15] Deposition numbers 2391599 (for [Ru]-m-benzene) contain the supplementary crystallographic data for this paper. These data are provided free of charge by the joint Cambridge Crystallographic Data Centre and Fachinformationszentrum Karlsruhe Access Structures service.

[16] D. Chen, Z. Pu, R. Lu, P. Ji, P. Wang, J. Zhu, C. Lin, H. W. Li, X. Zhou, Z. Hu, F. Xia, J. Wu, S. Mu, *Adv. Energy Mater.* **2020**, *10*, 2000814.

[17] Y. Yue, G. Hu, M. Zheng, Y. Guo, J. Cao, S. Shao, *Carbon* **2012**, *50*, 107–114.

[18] a) Y. Cui, S. Zhang, X. Zhou, F. Yan, W. Hu, *Microchem. J.* **2023**, *190*, 108632; b) F. A. Bushira, S. A. Kitte, H. Li, L. Zheng, P. Wang, Y. Jin, *J. Electroanal. Chem.* **2022**, *904*, 115956.

[19] a) Z. Zhou, S. Mukherjee, S. Hou, W. Li, M. Elsner, R. A. Fischer, *Angew. Chem. Int. Ed.* **2021**, *60*, 20551–20557; b) S. Vinoth, P. Mary Rajaitha, A. Pandikumar, *Compos. Sci. Technol.* **2020**, *195*, 108192; c) E. Laviron, *J. Electroanal. Chem.* **1974**, *52*, 355–393.

[20] B. Kulyk, S. O. Pereira, A. J. S. Fernandes, E. Fortunato, F. M. Costa, N. F. Santos, *Carbon* **2022**, *197*, 253–263.

[21] X. Wei, Y. Lin, Z. Wu, Y. Qiu, Y. Tang, M. Eguchi, T. Asahi, Y. Yamauchi, C. Zhu, *Angew. Chem. Int. Ed.* **2024**, *63*, e202405571.

[22] a) M. J. Lee, K. Lee, J. Lim, M. Li, S. Noda, S. J. Kwon, B. DeMattia, B. Lee, S. W. Lee, *Adv. Funct. Mater.* **2021**, *31*, 2009397; b) G. Wang, J. Meng, H. Liu, S. Jiao, W. Zhang, D. Chen, B. Fang, *Electrochim. Acta* **2008**, *53*, 2837–2843.

[23] a) T. Lei, W. Chen, W. Lv, J. Huang, J. Zhu, J. Chu, C. Yan, C. Wu, Y. Yan, W. He, J. Xiong, Y. Li, C. Yan, J. B. Goodenough, X. Duan, *Joule* **2018**, *2*, 2091–2104; b) J. E. B. Randles, *Discuss. Faraday Soc.* **1947**, *1*, 11–19.

[24] a) G.-G. Fan, B.-W. Jiang, W. Sang, H. Cheng, R. Zhang, B.-Y. Yu, Y. Yuan, C. Chen, F. Verpoort, *J. Org. Chem.* **2021**, *86*, 14627–14639; b) Q. Yang, Y. Li, J. D. Yang, Y. Liu, L. Zhang, S. Luo, J. P. Cheng, *Angew. Chem. Int. Ed.* **2020**, *59*, 19282–19291.

[25] a) V. K. Rajan, C. K. Hasna, K. Muraleedharan, *Food Chem.* **2018**, *262*, 184–190; b) P. Rodríguez-Maciá, K. Pawlak, O. Rüdiger, E. J. Reijerse, W. Lubitz, J. A. Birrell, *J. Am. Chem. Soc.* **2017**, *139*, 15122–15134.

[26] a) X. Yang, J. Yi, T. Wang, Y. Feng, J. Wang, J. Yu, F. Zhang, Z. Jiang, Z. Lv, H. Li, T. Huang, D. Si, X. Wang, R. Cao, X. Chen, *Adv. Mater.* **2022**, *34*, e2201768; b) J. R. Sempionatto, M. Lin, L. Yin, E. De la Paz, K. Pei, T. Sonsa-Ard, A. N. de Loyola Silva, A. A. Khorshed, F. Zhang, N. Tostado, S. Xu, J. Wang, *Nat. Biomed. Eng.* **2021**, *5*, 737–748.

[27] a) M. Wang, Y. Yang, J. Min, Y. Song, J. Tu, D. Mukasa, C. Ye, C. Xu, N. Heflin, J. S. McCune, T. K. Hsiai, Z. Li, W. Gao, *Nat. Biomed. Eng.* **2022**, *6*, 1225–1235; b) J. Xiao, Y. Luo, L. Su, J. Lu, W. Han, T. Xu, X. Zhang, *Anal. Chim. Acta* **2022**, *1208*, 339843.

[28] a) F. Ambroz, T. J. Macdonald, V. Martis, I. P. Parkin, *Small Methods* **2018**, *2*, 1088173; b) B. Ravel, M. Newville, *J. Synchrotron Radiat.* **2005**, *12*, 537–541; c) H. Funke, A. C. Scheinost, M. Chukalina, *Phys. Rev. B* **2005**, *71*, 094110; d) H. Funke, M. Chukalina, A. C. Scheinost, *J. Synchrotron Radiat.* **2007**, *14*, 426–432; e) Hongzhiwei Technology, Device Studio, Version 2021 A, China, **2021**, Available online: https://ire-

search.net.cn/cloudSoftware; f) G. Kresse, J. Furthmüller, *Phys. Rev. B* **1996**, *54*, 11169–11186; g) G. Kresse, J. Furthmüller, *Comput. Mater. Sci.* **1996**, *6*, 15–50; h) P. E. Blochl, *Phys. Rev. B* **1994**, *50*, 17953–17979; i) Q. Yang, Y. Li, J. D. Yang, Y. Liu, L. Zhang, S. Luo, J. P. Cheng, *Angew. Chem. Int. Ed.* **2020**, *59*, 19282–19291; j) E. Alcalde, I. Dinarès, S. Rodríguez, C. Garcia de Miguel, *Eur. J. Org. Chem.* **2005**, *2005*, 1637–1643.

Manuscript received: January 7, 2025
Accepted manuscript online: February 17, 2025
Version of record online: February 25, 2025

[Correction added on 27.3.2025, after first online publication: Figure 2 and Figure 3 has been updated.]

Research Article

Single-Atom Catalyst

B. Jiang, H. Zhang, R. Pan, M. Ji, L. Zhu, G. Zhang, J. Liu, H. Shi, H. Huang, S. Wan, K. Yin,* L. Sun* ——— **e202500474**

Three-Electron Uric Acid Oxidation via Interdistance-Dependent Switching Pathways in Correlated Single-Atom Catalysts for Boosting Sensing Signals

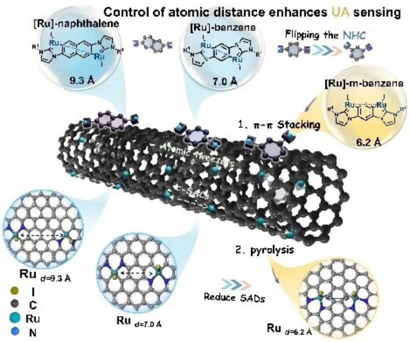

Correlated ruthenium single-atom catalysts (Ru c-SACs) with tailored single-atomic interdistance (SAD) of 9.3 Å, 7.0 Å, and 6.2 Å were prepared via organometallic design. The Ru c-SAC with 6.2 Å SAD exhibited superior uric acid electrooxidation activity due to the optimal inter-atomic distance facilitating a three-electron transfer pathway, substantiated by comprehensive experimental studies and theoretical computations, and unveiling atomic-level SAD-activity relationships in single-atom electrochemical sensing.